Experiments in Fluids 34 (2003) 1–15
DOI 10.1007/s00348-002-0447-2

Surfactant spreading on thin viscous films: film thickness evolution and periodic wall stretch

J.L. Bull, J.B. Grotberg

Abstract Surfactant spreading on thin viscous films is of interest in the context of surfactant and liquid transport in the lungs, for both normal lung function and treatment of disease, as well as for many industrial processes. This paper presents experimental techniques for the measurement of film deformations due to spreading surfactant and for the investigation of the effects of periodic stretching of the wall supporting the thin film to mimic airway wall motion in the lung due to breathing. Additionally, we present results from both types of experiments, which agree favorably with our theoretical work.

List of symbols

Bo	Bond number
D_s	surface diffusivity
g	acceleration due to gravity
h	film thickness
h_0	initial film thickness
L_d	radial position of surface compression disturbance
L_0	initial radial position of leading edge of new surfactant front
L_{new}	radial position of new surfactant front
p	pressure
Pe	Péclet number
R	membrane well radius
R_0	initial membrane well radius
$\hat{R}$	R_0/L_0, non-dimensional initial membrane well radius (same as cycle average well radius)
Re	Reynolds number
t	time
T_C	stretching cycle period
$T_{C/V}$	ratio of stretch time scale to viscous-surface-tension time scale
T_V	viscous-surface-tension time scale
u	radial velocity
U	viscous-surface-tension velocity scale
w	vertical velocity
x	radial coordinate
z	vertical coordinate
α	shape parameter for initial surfactant distribution
Δh	film thickness deformation
Δx	horizontal shift in grid position
ϵ	aspect ratio
Γ	surfactant surface concentration
Γ_{ref}	reference surfactant surface concentration
Γ_0	pre-existing surfactant initial surface concentration
Γ_1	new surfactant initial surface concentration
η	refractive index of fluid
μ	viscosity
θ	angle of incidence
ρ	density
σ	surface tension
σ_{max}	maximum surface tension
ξ	membrane wall coordinate

Superscripts

$*$	indicates dimensional variable (note that dimensional parameters have no asterisk)

Received: 20 September 2000 / Accepted: 15 March 2002
Published online: 19 October 2002

J.L. Bull (✉), J.B. Grotberg
Biomedical Engineering Department,
The University of Michigan, Ann Arbor, MI 48109, USA
E-mail: joebull@umich.edu

This work was supported by NIH grant HL-41126 and NSF grant CTS-9412523. We wish to thank Dr Steve Ceccio for generously allowing the use of laboratory equipment. Thanks are also due to Dr Matthew R. Glucksberg and Dr Christopher Waters for use of their cell-stretching device.

1 Introduction

The transport of surfactants on thin viscous films and the resulting film deformations are of concern in the treatment of respiratory distress syndrome (RDS), in which the lungs of prematurely born infants are not developed enough to produce sufficient quantities of surfactant to reduce the surface tension of the lungs' liquid lining. In surfactant replacement therapy (SRT), surfactant is instilled into the trachea of a patient with surfactant-deficient lungs and it is transported in the large airways primarily by gravity and pressure (Halpern et al. 1998a; Espinosa and Kamm 1999). As the surfactant layer thins to a monolayer, Marangoni flows become the dominant mode of transportation (Halpern et al. 1998a; Espinosa and Kamm 1999). Surface-tension-driven flows are also important in the clearance of liquid and surfactant from healthy lungs (Davis et al. 1974; Espinosa and Kamm 1997; Bull 2000).

Transient spreading of surfactant along a thin viscous film has been studied theoretically (Borgas and Grotberg 1988; Gaver and Grotberg 1990; Troian et al. 1990; Halpern and Grotberg 1992; Jensen and Grotberg 1992; Espinosa et al. 1993; Jensen and Grotberg 1993; Grotberg 1994; Jensen et al. 1994; Shen and Hartland 1994; Grotberg et al. 1995; Bull et al. 1999) and, to a much lesser extent, experimentally (Weh and Linde 1973; Keshgi and Scriven

1991; Gaver and Grotberg 1992; Bull et al. 1999). When an insoluble surfactant spreads on an otherwise clean thin film, a shock develops near the leading edge of the new surfactant front. A sketch of this is shown in Fig. 1. Figure 1a shows the initially flat film with new surfactant on the left side. When gravity is negligible, the film thickens to twice its undisturbed thickness (Borgas and Grotberg 1988; Gaver and Grotberg 1990; Grotberg 1994) at the shock and thins behind the shock, as shown in Fig. 1b. Thickening of the liquid lining the airways can lead to airway closure, in which a disturbance grows to the point of occluding the airway (Halpern and Grotberg 1993a; 1993b; Halpern et al. 1993; Halpern et al. 1998b; Cassidy et al. 1999; Halpern and Grotberg 1999). Additionally, the film thinning can result in film rupture (Weh and Linde 1973; Keshgi and Scriven 1991; Gaver and Grotberg 1992; Bull et al. 1999), which would halt the spreading of new surfactant and dry underlying tissue, in SRT, unwanted results. There appear to be no other experimental investigations of this film deformation in the current literature. In this paper, we present a constructed-light method for measuring film thickness in surfactant-spreading experiments. This method requires minimal equipment and involves projecting a grid of light onto the film surface to determine the film deformation. Another film deformation involving surfactant, the Reynolds ridge, has been studied extensively (Harper and Dixon 1974; Scott 1982; Warncke et al. 1996). While the mechanism responsible for the production of the Reynolds ridge differs from the mechanism that produces the film deformation in this work (discussed in Sect. 5.1), the experimental techniques used to study the Reynolds ridge

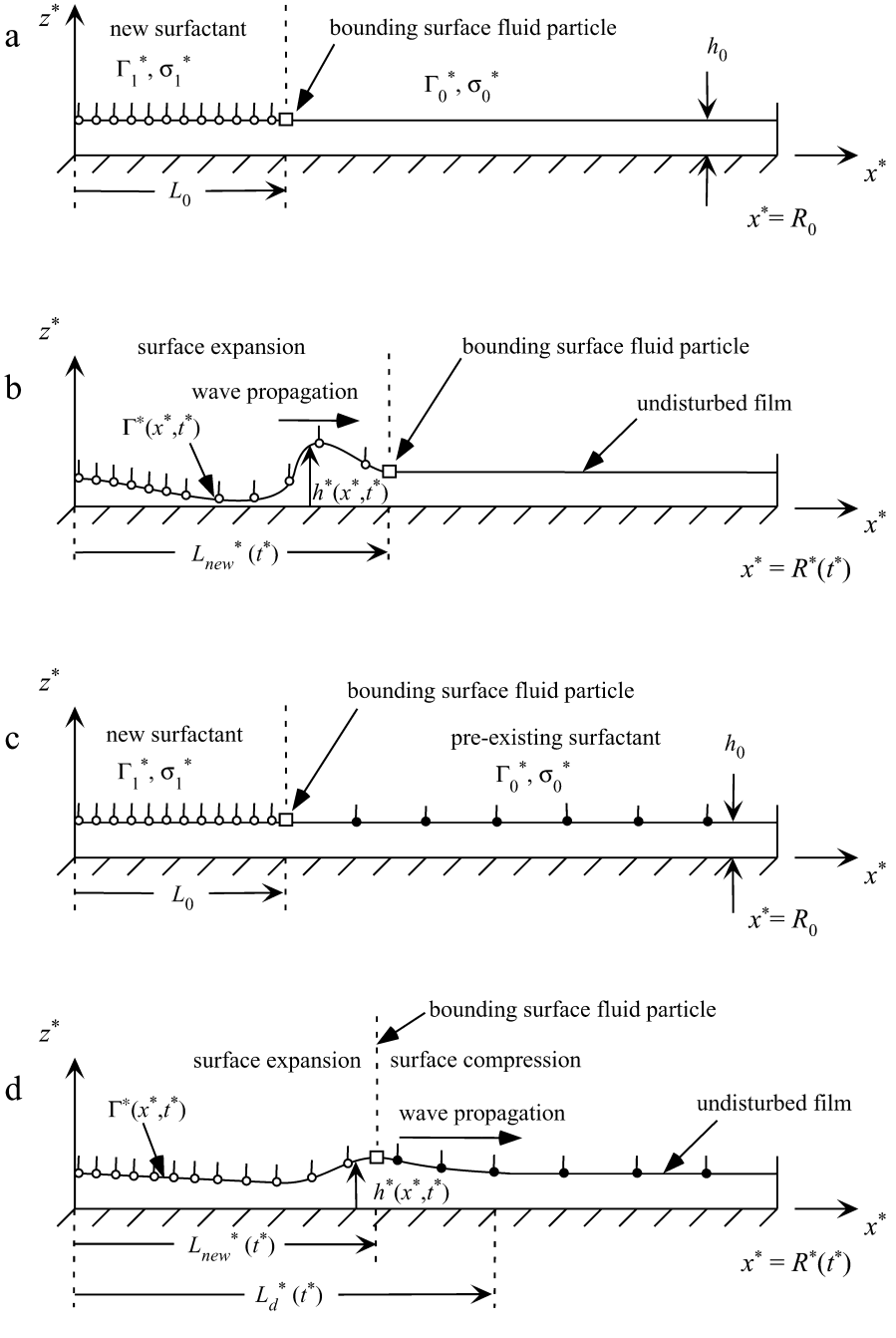

Fig. 1a–d. Schematic of thin film with surfactant, side-view, *open square* indicates the surface fluid particle that bounds the new surfactant region. The radial location of this position of this particle is $x^*_{\text{new}}(t^*)$. Film thickness, $h^*(x^*,t^*)$, and surfactant surface concentration, $\Gamma^*(x^*,t^*)$, evolve as new surfactant spreads. **a** Initially uniform film with new surfactant and no pre-existing surfactant. **b** Film disturbance at later time, while new surfactant spreads. **c** Initially flat film with new surfactant (*unfilled*) and pre-existing surfactant (*filled*). **d** Film at later time. New surfactant has expanded, and pre-existing surfactant is compressed. Location on compression disturbance is indicated by $x^*_{\text{d}}(t^*)$

could be used to investigate the film deformation described here.

Pre-existing surfactant impedes the spreading of new surfactant and leads to a surface compression disturbance that propagates faster than the leading edge of the new surfactant front (Grotberg et al. 1995; Bull et al. 1999). The surface compression disturbance could potentially be important clinically, as it increases the surface concentration of surfactant in regions distal to the new surfactant, some of which may not be reached by the new surfactant. Figure 1c shows an initially flat film with new surfactant on the left side (shown as unfilled surfactant molecules) and pre-existing surfactant (shown as filled surfactant molecules). When the new surfactant spreads, the pre-existing surfactant becomes compressed ahead of the leading edge of the new surfactant front, as shown in Fig. 1d. The location of the leading edge of the new surfactant is indicated by the particle that separates the new and the pre-existing surfactant. Note that the surface compression disturbance, L_d^*, is ahead of L_{new}^*. Behind L_d^*, the pre-existing surfactant is compressed, while the new surfactant region is expanded. Ahead of L_d^*, the pre-existing surfactant surface concentration is unchanged. In addition to impeding the new surfactant spreading, the pre-existing surfactant damps the thickness disturbance compared to the case of no pre-existing surfactant. However, there remains a potential for this thickness disturbance to lead to airway closure or film rupture.

Bull (2000) theoretically examined mean-steady transport of liquid and surfactant in the lung with periodic wall stretch due to breathing and found that transport of liquid and surfactant is significantly influenced by the strain amplitude and cycling period of the periodic wall stretch. Espinosa and Kamm (1997) examined the redistribution of liquid on a stretchable membrane due to surface tension-driven flows as a model of liquid transport in the lung. They found that the thickness profile of liquid on a stretchable membrane with end-walls changes in the first few cycles of stretch.

Previous work in this area has been theoretical and it appears that there are no previous experimental studies of surfactant (liquid) transport on (in) a film supported by a stretchable wall in the current literature. In addition to the film deformation measurement method mentioned earlier, this work presents an experimental method for investigating thin films supported by a stretchable wall and examines transient surfactant spreading on a thin film with periodic wall stretch. We use a stretching device which has been used to investigate the effects of stretch on cell growth, but has not previously been used to investigate wall stretch effects related to fluid mechanics. The model of Bull (2000) is modified such that the boundary conditions, initial conditions, and geometry match these experiments, and the results are compared.

2
Methods

2.1
Overview of experiments

The bench top experiments in this work were conducted in a similar manner to those described in (Bull et al. 1999), with the additional complication of measuring film thickness or of wall stretch. Both experiments examine the spreading of surfactant on a thin film. A brief overview of the experiments is as follows. Glycerine forms a thin viscous film in either a glass petri dish or in a well on a stretchable membrane. Initially, 'new' surfactant is contained at a uniform concentration inside a glass restraining collar and the film outside the collar is either surfactant free (Fig. 1a) or contains pre-existing surfactant at a uniform surface concentration, Γ_0^*, lower than that inside the collar (Fig. 1c). The center of the restraining collar is located at the center of the dish, $x^*=0$. The side-view of one half of the film is shown in Fig. 1. The air–liquid interface is denoted by $z^*=h^*(x^*, t^*)$, where t^* is time. At the start of the experiment, the collar is lifted and the new surfactant spreads, compressing any pre-existing surfactant and causing the film height to deform, as shown in Fig. 1b and d. In the wall stretch experiments, the periodic wall stretch starts when the collar is lifted. The film deformation is measured using a constructed-light method, or the propagation of the leading edge of the surfactant front is tracked using the fluorescence properties of the new surfactant. We describe the surfactant properties in Sect. 2.2. While fairly routine, the procedure for cleaning the collar is described in Sect. 2.3, as a minimal amount of impurities is necessary to obtain consistent results. We discuss the film thickness measurements in Sect. 2.4 before explaining the methodology for the wall stretch in Sect. 2.5.

2.2
Surfactant properties

The surfactants used here are the same as in Bull et al. (1999). Hence, the same surfactant isotherm of Bull et al. (1999) is used. The process of determining the surfactant isotherm is summarized in the next few paragraphs. The new surfactant used here is a fluorescent analogue of phosphatidylcholine, 1–16:0–2-[12-[(7-nitro-2–1,3-benzoxadiazol-4-yl)amino]dodecanoyl] phosphatidylcholine (abbreviated as NBD-PC), purchased from Avanti Polar Lipids (Alabaster, Ala.). NBD-PC was contained in a chloroform solution at a concentration of 1.0 mg/ml, allowing it to be placed on the surface of the glycerine film with a micro-liter syringe. The broad excitation peak at 460 nm of NBD-PC allows emission at a peak of 534 nm to be stimulated by an argon ion laser. In addition to its fluorescent properties, NBD-PC was chosen because it exhibits surface-active properties at room temperature. The precursor molecule to NBD-PC without the fluorescent probe, palmitoyl-lauroyl-sn-glycero-3-phosphocholine (PL-PC), was used as the pre-existing surfactant in these experiments (when such was used).

The measurements of surface tension were made using the ring tensiometer method (see, for example, Adamson 1990 for more details of the method) as described in Bull et al. (1999). The theoretical model, described in Sect. 3 requires the first and second derivatives of the σ^*–Γ^* relationship as inputs. Consequently, accurate measurement of $\sigma^*(\Gamma^*)$ is necessary for meaningful comparison between experiments and theory. The force required to detach a platinum ring from the surface of glycerine in a

petri dish was measured for various surface concentrations of NBD-PC and PL-PC. A platinum ring was attached with light-weight thread to a Mettler AE240 mass balance (Columbus, Ohio) with an accuracy of 0.1 mg. A data acquisition program on a Intel 486 PC connected to the balance was used to store the mass balance measurements throughout the experiment so that an accurate maximum value of the force required to detach the ring from the liquid surface could be obtained. The petri dish containing the glycerine sublayer and a specified amount of surfactant was placed on an adjustable platform. Initially, the ring was submerged in the glycerine sublayer and the mass balance set to zero to account for the weight of the ring-and-thread assembly. As the platform was lowered slowly, the readings on the mass balance steadily increased until the ring detached from the liquid. From a force balance on the ring, one can calculate the surface tension.

This process was repeated for various surface concentrations of surfactant to obtain a plot of σ^* versus Γ^*. The surface concentrations in the experiments were sufficiently low that it was assumed that no surfactant leaves the interface, so that surface concentration, Γ^*, was calculated by $\Gamma^*=M^*/A^*$, where M^* is mass of surfactant and A^* is surface area. However, for high-enough Γ^*, it is quite likely that surfactant would leave the surface and enter the bulk fluid. Solubility of the surfactants in the bulk phase could result in error in the σ^*–Γ^* for high values of Γ^*. The results from these experiments are plotted with surface tension as a function of surfactant surface concentration in Fig. 2. Measurements for both the pre-existing and new surfactants used in the spreading experiments were compared. Since the plots were not significantly different from each other, the surface tension values for the initial pre-existing surfactant concentration along with the pre-existing concentrations were approximated from a single calibration curve. This curve, represented by the measurements for the new surfactant, is shown in Fig. 2 for the range of initial surface concentration values used in the experiments ($\Gamma^*\approx 0$ to 4.2×10^{-7} g/cm^2, the asterisk indicates dimensional variables). The following equation was used for the σ^*–Γ^* relationship:

$$\begin{aligned}&\sigma^* = 9.380\cos(2.094\Gamma^*) + 59.069,\ \Gamma^* < 0.75\\ &\sigma^* = 77.084 - 28.677\Gamma^* + 6.588\Gamma^{*2} - 0.5042\Gamma^{*3},\\ &0.75 \le \Gamma^* \le 5.0\end{aligned} \qquad (1)$$

In the spreading experiments, the surfactants were allowed to reach uniform concentrations inside and outside the collar before lifting the collar to begin the experiments. To estimate the time required for surfactant surface concentration to equilibrate, surface tension measurements were taken at different positions in a petri dish at 10-min time intervals until the measurements were within 5.0% of each other, which occurred after 30 min. By waiting 1 h after placing the surfactants on the glycerine film, we were assured of relatively uniform initial surfactant concentrations both inside and outside (lower concentration) the collar.

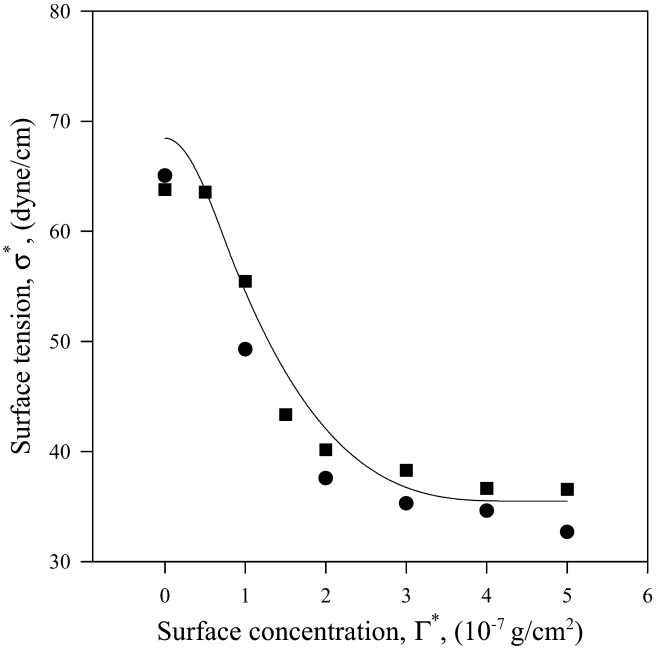

Fig. 2. Surface tension versus surface concentration curves. Experiments: PL-PC *solid circle*, NBD-PC *solid square*, regression *dashed line*

2.3 Cleaning procedure

As surface impurities can change the surface tension of the liquid and can result in liquid and surfactant adhering to the restraining collar in the spreading experiments, it was essential to thoroughly clean the equipment before each experiment. The cleaning procedure is as follows. The petri dish (or Silastic membrane) and glass restraining collar were washed with soapy water. The collar was rinsed with benzene, acetone, and chloroform. It was allowed to dry before being rinsed with the next chemical. This rinsing procedure was performed twice prior to cleaning in chromic acid. The collar was rinsed with tap water and deionized-distilled water and air dried. The petri dish was cleaned in the same way as the collar for each experiment. Dust was blown with compressed medical-grade air from the collar and petri dish immediately before placing the glycerine. The micro-liter syringe used for deposition of the surfactants was rinsed with chloroform before and between experimental runs.

2.4 Film thickness measurements

Before beginning an experiment, paper with marker lines to aid in collar placement was placed beneath a glass petri dish on a leveling platform. A specified volume of glycerine, corresponding to the initial film thickness of h_0, was placed in the petri dish with a syringe. After any thickness disturbances due to the filling process had equilibrated, a 30-mm-diameter glass restraining collar was placed at the center of the dish. A specified amount of NBD-PC corresponding to the desired initial new surfactant surface concentration was placed inside the collar with the micro-liter syringe. After the surfactant had reached its equilibrium surface concentration, the experiment was started by lifting the collar. The thin film was

videotaped using a Video Logic Color Star 300 video camera (Panasonic, Osaka, Japan) and JVC SR-S360 S-VHS video recorder (JVC, Tokyo, Japan) until spreading had stopped. Glycerine formed the viscous liquid sublayer in these experiments. After each experiment, the viscosity of the glycerine was measured using an bulb viscometer (Cannon-Fenske-Oswald type 400 J788). To ensure that no surfactant adhered to the collar, we viewed it under the laser with a Hammamatsu Argus 20 camera and image processor (Hammamatsu, Hammamatsu City, Japan), integrating over 1 min following several experiments to assure that surfactant did not adhere to it. Provided the restraining collar was cleaned using the procedure outlined in Sect. 2.3 prior to placing it on the interface and placing the surfactants, we observed no surfactant on the collar following the spreading experiments. Since no detectable surfactant adsorbed onto the collar, we assumed that none absorbed onto the wall of the petri dish.

A constructed-light method was used to measure the film thickness. This method involves projecting a grid of lines onto the surface of the film, as shown in Fig. 3a, and observing the deformation of the lines. The refractive index of glycerine is $\eta \approx 1.47$, which is approximately the same as that of the glass dish on which the glycerine rests. Thus, the reflection from the surface of the film is the image that is detected by the camera. The lines will bend where the film is non-uniform. From geometry (see Fig. 3b), we see that the amount a line appears shifted depends on the angle at which it is projected onto the film and the deformation of the film by $\Delta x^* = \Delta h^* \tan\theta$, where Δx^* is the deflection observed in the reflected line, Δh^* is the change in film thickness, and θ is the projection angle relative to vertical. The projector setup used here was simple. A grid of lines was printed on a transparency using a laser printer (Hewlett Packard, Laser Jet 5MP; Hewlett Packard, Boise, Idaho) and an overhead projector was used to project the lines onto the glycerine film. The angle, θ, was measured using a protractor and plumb bob attached to the lens of the projector. It was possible to focus the projector such that all of the lines were in focus. The video tape images were captured to a computer using the software Targus Capture (Truevision, Indianapolis, Ind.). The images were analyzed using Sigmascan (SPSS Scientific, Chicago, Ill.) and accurate measurements of Δx^* were obtained at each grid line at a given time. These values of Δx^* were then used to compute the value of Δh^* at each grid line. Knowing these values and the undisturbed film thickness, h_0, one can compute $h^*(x^*, t^*)$ at a given instant in time.

2.5 Wall stretch experiments

2.5.1 Membrane construction

The materials used in the experiments with the stretchable membrane are the same as in the experiment described in Sect. 2.4, except here the glass petri dish is replaced by a stretchable membrane. The membrane was made of Silastic (Dow Corning, Midland, Mich.), which is a silicon-based elastic. A Silastic membrane is constructed by mixing the base and curing agents for the elastic and then pouring them into a mold. Curing of the Silastic typically takes 24 h or slightly longer. The curing process can be expedited by heating the Silastic while it cures. However, this was not done for the membranes used to obtain results, as slower curing allows sufficient time for any air bubbles in the Silastic to escape. Trapped air bubbles can cause non-uniformities in the strain field and cause difficulty in visualizing grid markers underneath the membrane. The membranes used in the experiments were constructed in the following manner.

A thin (~1 mm thick) cylindrical (~9.5 cm diameter) wall was first made by coating the inside of a plastic cylinder with the liquid Silastic and allowing it to cure. At the same time, a larger flat section was poured approximately 1.5 mm thick. Any detected air bubbles were punctured with a 16-gage needle and the Silastic was allowed to cure.

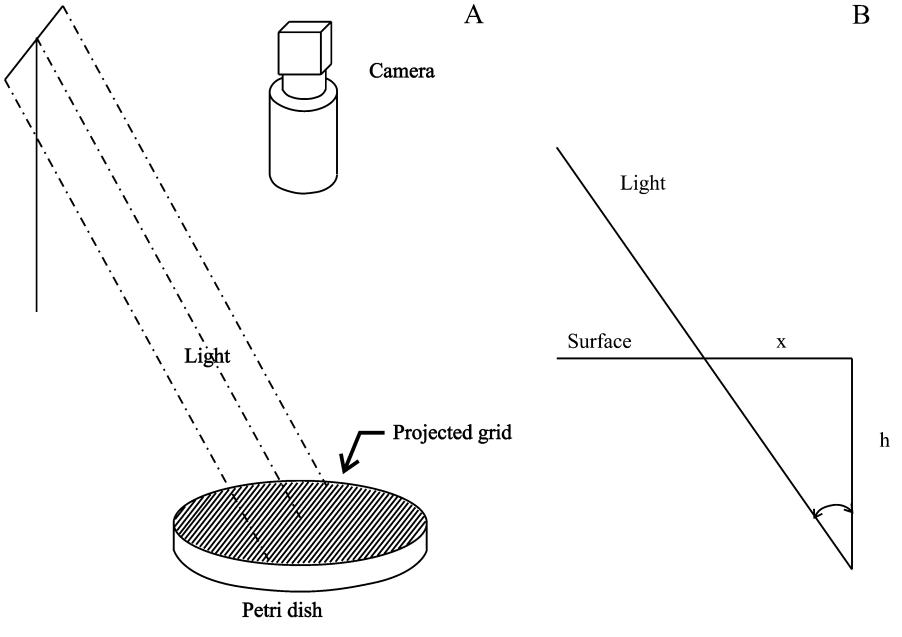

Fig. 3a, b. Constructed-light thickness measurement. a Side-view of setup. Light is projected onto the glycerine film at angle θ to the vertical and imaged with ccd camera above the film. b Geometry for calculation of film deformation, Δh, based on observed grid deformation, Δx

After 24 h, the cylinder was trimmed to a height of approximately 1 cm and a section resembling a square with rounded corners was cut from the center of the flap.

Next, another flap was poured. Prior to placing the Silastic into the mold, a grid was constructed by printing a grid on a laser printer transparency. The transparency was removed from the printer (Hewlett Packard, Laser Jet II) before the printing process completed, leaving toner particles on the transparency in the shape of the grid. This transparency was then placed printed side up in the bottom of the mold and the Silastic for the second flap was placed in the mold. After allowing the flap to cure for several hours and removing air bubbles as previously described, we placed the previously constructed flap with cut-out on top of the freshly poured flap. Then the thin cylindrical wall was placed in a vertical position such that it extended approximately half way into the flap. The cylindrical wall was held in place by allowing it to protrude from the end of the plastic tube used to mold it and the tube was then positioned using a Leitz micro-manipulator (Ernst Leitz, Wetzlar, Germany). After the flap had cured, it was removed from the mold and the transparency was removed from the bottom of the flap, leaving the grid on the membrane. This resulted in a stretchable membrane as shown in Fig. 4. The vertical wall formed a cylindrical well, in which the glycerine layer was placed. The grid on the membrane allowed the collar to be placed at the center of the well with reasonable precision and was useful in determining when the radius of the well was at its mean value.

We were able to obtain a membrane that resulted in a strain field that was approximately uniform, when the membrane was loaded biaxially. The strain in the membrane was estimated to be uniform by making use of various lines placed on the membrane, using the laser printer transparency as described above. A uniformly thick, square membrane will undergo uniform strain when subjected to a uniformly distributed loading along each of the four edges. This is a good approximation of the membrane loaded as in the experiments, and efforts were made to reduce stress concentrations by rounding the corners of the membrane and to reduce deformation of the wings that attached in the stretching device.

2.5.2 Experimental apparatus

A sketch of the membrane in the stretching apparatus is shown in Fig. 4 from the top view. The device consists of a base plate to which the slider plates, the membrane clamps, and the pneumatic cylinders are attached. The membrane is clamped to the stretching device and the motion of the slider plates is controlled by the pneumatic cylinders, causing the top and right (relative to the sketch in Fig. 4) edges of the membrane to move. Consequently, the center of the membrane oscillates about its mean location during the stretching process. The motion of the pneumatic cylinders is controlled by computer-controlled servo regulation of pneumatic valves in the lines that connect the pneumatic cylinders to the air compressor (not shown). A BASIC program on an Intel 486 PC controlled the periodic stretching of the membrane, and the frequency and strain amplitude were set for each experiment. A trigger attached to the base plate triggered the shutter on the 35-mm camera at the start of every

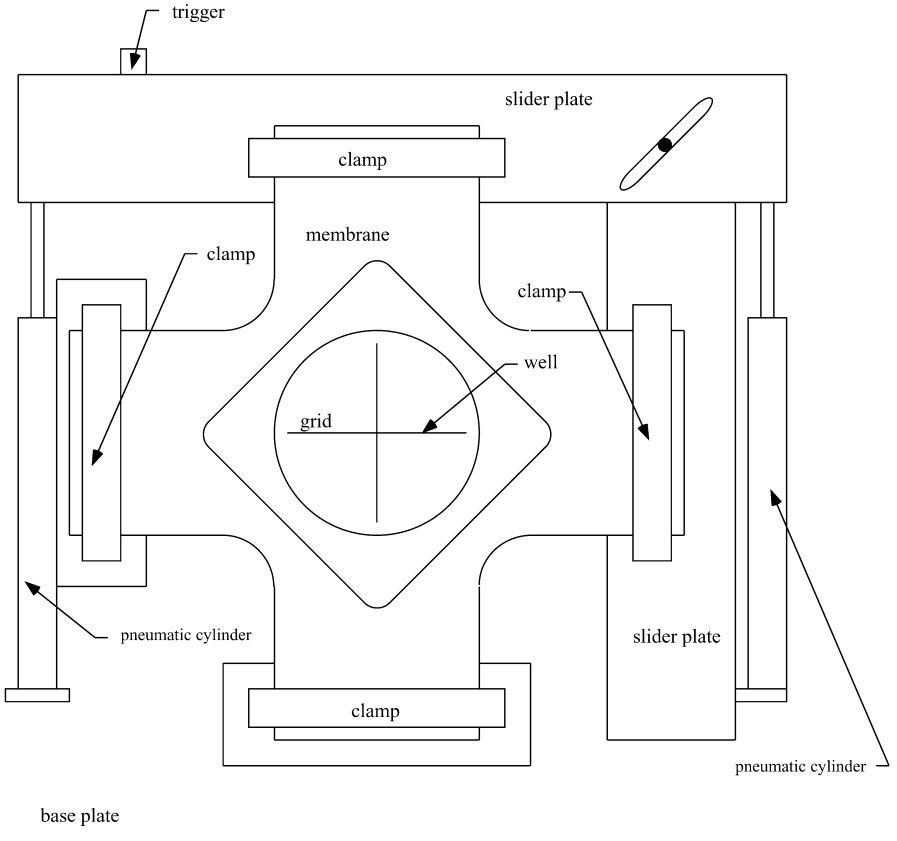

Fig. 4. Top-view of stretching apparatus with membrane. The pneumatic cylinders move the slider plates causing the membrane to stretch

stretching cycle (when the membrane well was at its mean radius).

2.5.3
Experimental procedure

The procedure for the stretching experiments is similar to the procedure for the thickness measurements, as described in Sect. 2.4, except the wall supporting the film stretches periodically and we track the leading edge of the new surfactant front using a laser rather than measure film thickness. Before beginning the experiments, the optics were blown with clean dry air to clear away any dust or dirt particles. The membrane was stretched to its mean radius and a specified volume of glycerine corresponding to an experimental value of h_0, the initial film height, was deposited in the membrane well with a plastic syringe. A specified amount of NBD-PC was placed inside the collar. The amount of PL-PC corresponding to the desired concentration of pre-existing surfactant was placed outside the collar. The collar restrained the NBD-PC until the chloroform had evaporated. The surfactants were allowed to reach a uniform concentration inside and outside the collar by waiting 1 h (as discussed in Sect. 2.2) before beginning the transient spreading. Hence, the new surfactant region had a uniform initial surface concentration, and a uniform and consistent initial radius. The region outside the collar had a uniform initial concentration of pre-existing surfactant.

The tunable argon ion laser (Lexel Model 95, Fremont, Calif.) was set to emit at its maximum power of 1 W at 488 nm, thus allowing for maximal excitation of the fluorescent surfactant. This allowed for excitation of the fluorescent surfactant, while not contributing detectable light in the emission band of the fluorescent surfactant. A filter (Mieles Griot OG550, Carlsbad, Calif.) mounted to the 35-mm SLR camera lens (Nikon, Tokyo, Japan) blocked light below a wavelength of 550 nm and therefore allowed most of the fluorescence from the spreading surfactant and surface markers to penetrate while blocking the argon laser light.

The laser beam was directed to the experimental setup shown in Fig. 5 using mirrors. The beam was projected onto the glycerine surface by a scanner. The scanner consisted of an oscillating mirror driven by a 120-Hz sine wave from a signal generator (Wavetek Precision Measurement, Norwich, UK). A potentiometer was used to adjust the base angle of the scanner mirror and direct the beam toward the membrane well. The scanned laser beam was kept within the edges of the membrane well (to minimize any reflectance of the light from the sides) by adjusting the amplitude of the 120-Hz sine wave.

After the surfactants had reached equilibrium surface concentrations (Γ_1^* inside the collar and Γ_0^* outside the collar), the experiment was started by simultaneously lifting the collar and beginning the periodic stretching of the membrane. Because the surface concentration was initially higher in the new surfactant region than in the pre-existing surfactant region (and hence, the surface tension is initially lower in the new region than in the pre-existing region), the new surfactant spread, compressing the pre-existing surfactant. The periodic wall stretch influences surfactant spreading by modifying the surface tension gradients and cycling the film thickness of the entire film. The experiment was conducted at different frequencies and pre-existing surfactant concentrations to gain insight into the influence of breathing on Marangoni-driven surfactant spreading in SRT. As mentioned in Sect. 2.4, we imaged the collar illuminated by the laser after the completion of the experiments to ensure that surfactant had not adhered to the collar. Using a Hammamatsu Argus 20 camera and image processor, we integrated the video over 1 min. Traces of surfactant were not found.

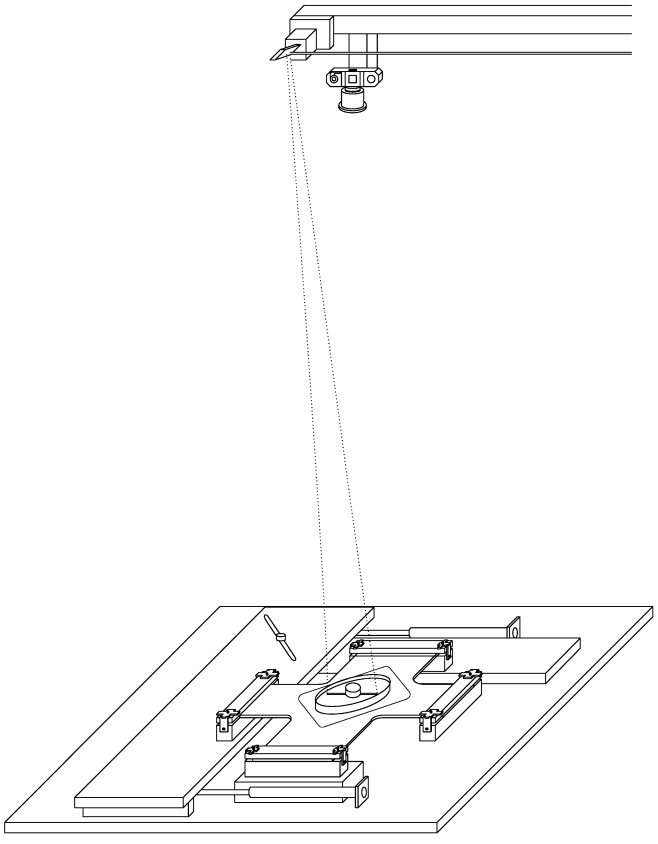

Fig. 5. Experimental setup

2.6
Limitations and possible error sources

Although many steps were taken to control the initial conditions and minimize surface contamination, there are some possible sources of error in these experiments. There is the possibility that the plastic syringe (with rubber plunger) used to place the glycerine could have resulted in contamination. Likewise, it is possible that surfactants leached from the Silastic membrane into the glycerine. We expect that errors due to the Silastic membrane were small because the no-stretch results using the membrane agree well with a similar configuration that used a glass petri dish. Another possible source of contamination is the air used to remove dust from the restraining collar and dish. We expect that the medical-grade air had a low enough concentration of any surface-active impurities that any effects were negligible. While we took considerable steps to

ensure that surfactant did not adhere to the glass restraining collar, it is possible that surfactant adsorbed onto the walls of the petri dish or membrane well. This would have resulted in a lower pre-existing surfactant concentration than expected based on the mass of PL-PC used. Since no surfactant was observed to adsorb onto the restraining collar, we did not expect substantial amounts of surfactant to adsorb onto the walls of the petri dish.

3 Model

Consider a thin viscous film bounded by a vertical circular wall centered on a horizontal square membrane subject to biaxial loading. Let the horizontal axis, x^*, lie along the surface of the membrane in the radial direction and the vertical axis, z^*, extend up normal to the membrane, as in Fig. 1. Note that variables with stars are dimensional, and parameters and dimensionless variables are un-starred. The fluid is bounded by a vertical wall attached to the membrane at $x^*=R^*(t^*)$ and is axisymmetric about $x^*=0$. The position of the film surface is defined as $z^*=h^*(x^*, t^*)$, the surface concentration of the surfactant is denoted by $\Gamma^*(x^*, t^*)$. The spreading of a new surfactant monolayer, initial length L_0, in the presence of pre-existing surfactant and periodic wall stretch is investigated. The cycle average and initial radius of the membrane well is R_0.

The governing equations for the fluid are conservation of linear momentum and conservation of fluid mass

$$\rho\left(\frac{\partial \mathbf{v}^*}{\partial t^*}+\mathbf{v}^*\cdot\nabla^*\mathbf{v}^*\right)=-\nabla p^*+\mu\nabla^{*2}\mathbf{v}^*+\rho g^*,\ \nabla^*\cdot\mathbf{v}^*=0 \tag{2}$$

where v^* is the velocity vector, t^* is time, p^* is pressure, and g^* is acceleration due to gravity. The governing equation for the surfactant is conservation of surfactant mass

$$\frac{\partial \Gamma^*}{\partial t^*}+\nabla_s^*\cdot(\mathbf{v}_s^*\Gamma^*)-D_s\nabla_s^{*2}\Gamma^*+(\nabla_s^*\cdot\mathbf{n})(\mathbf{n}\cdot\mathbf{v})\Gamma^*=0, \tag{3}$$

where $q^*(x^*, t^*)$ is the dimensional surface surfactant flux, ∇_s^* is the surface gradient operator, and v_s^* is the surface velocity. The surfactant may diffuse along the interface with constant diffusivity, D_s, or be convected along the surface.

The stress boundary condition at the air–liquid interface, $z^*=h^*$, representing the balance of viscous stress at the interface with the surface tension gradient and relating the capillary forces to the surface curvature; and the kinematic boundary condition at the air–liquid interface, $z^*=h^*$, requiring fluid particles initially on the interface to remain on the interface, are given by

$$\left[T_{ij}n_j\right]^*=\frac{\partial\sigma^*}{\partial s^*}\tau_i^*+\kappa*\sigma*n_i^*,\quad \frac{\partial(x^*h^*)}{\partial t^*}+\frac{\partial(x^*Q^*)}{\partial x^*}=0 \tag{4}$$

where T_{ij} is the stress tensor, n_i is the normal, τ_i is the surface tangent vector, $\partial\sigma^*/\partial s^*$ is the directional derivative of surface tension along the interface, κ^* is surface curvature, and $Q^*(x^*, t^*)=\int_0^{h^*}u^*\mathrm{d}y^*$ is fluid flux. The kinematic boundary conditions on the membrane surface, $z^*=0$, are no slip and no penetration,

$$\begin{aligned}u(x^*, z^*=0, t^*)&=V_{\mathrm{wall}}^*(x^*, t^*)\\ w(x^*, z^*=0, t^*)&=0\end{aligned} \tag{5}$$

where V_{wall}^* is the membrane wall velocity. We impose no slip and no penetration at the vertical wall of the well, $x^*=R^*(t^*)$, and impose symmetry at the center of the well, $x^*=0$.

The governing equations are scaled using the following scales:

$$\begin{aligned}&x^*=L_0x,\ \ z^*=h_0z,\ \ \sigma^*=\sigma_{\max}\sigma,\ \ \Gamma^*=\Gamma_{\mathrm{ref}}\Gamma\\ &u^*=Uu=\frac{\sigma_{\max}h_0}{\mu L_0}u,\ \ w^*=\frac{h_0U}{L_0}w,\\ &t^*=T_{\mathrm{V}}t=\frac{\mu L_0^2}{\sigma_{\max}h_0}t,\ \ P^*=\frac{\sigma_{\max}}{h_0}P\end{aligned} \tag{6}$$

where $\sigma_{\max}$ is the maximum surface tension, Γ_{ref} is the reference surface concentration, μ is fluid viscosity, u is radial velocity, w is vertical velocity, U is the velocity scale, T_{V} is the time scale from the balance of shear stress and surface tension gradients at the interface, and P is pressure. The dimensionless parameters are the aspect ratio, $\epsilon=h_0/L_0$; Reynolds number, $Re=\rho U L_0/\mu$; Bond number, $Bo=\rho h_0^2 g/\sigma_{\max}$; strain amplitude, Δ; non-dimensional cycling period, $T_{\mathrm{C/V}}=T_{\mathrm{C}}/T_{\mathrm{V}}$; non-dimensional well radius, $\hat{R}=R_0/L_0$; and surface Péclet number, $Pe=UL_0/D_s$, where g is acceleration due to gravity, T_{C} is the period of the wall oscillation, L_0 is the initial radius of the new surfactant region, and D_s is surface diffusivity. The dimensional and non-dimensional parameters for the experiments are contained in Tables 1 and 2, respectively. From the governing equations, the non-dimensional velocity fields and evolution equations are derived as in (Bull 2000). Considering the lubrication approximation ($\epsilon\to0$) and

Table 1. Dimensional parameter values

Dimensional parameter	Symbol	$\Gamma_0^*=0$	$\Gamma_0^*=1.77\times10^{-7}$ g/cm^2	$\Gamma_0^*=3.38\times10^{-7}$ g/cm^2
Initial film height, cm	H_0	0.2	0.2	0.2
Initial radial length, cm	L_0	1.5	1.5	1.5
Surface diffusivity	D_s	≈0	≈0	≈0
Surface tension (outside collar), dyne/cm	$\sigma^*{}_0$	68.5	44.17	35.95
Surface tension in new Surfacant region, dyne/cm	$\sigma^*{}_1$	35.50	35.50	35.50
Time scale, s	T_{V}	0.71	0.71	0.71

Table 2. Dimensionless parameter values

Dimensional parameter	Symbol	$\Gamma_0^*=0$	$\Gamma_0^*=1.77\times10^{-7}$ g/cm^2	$\Gamma_0^*=3.38\times10^{-7}$ g/cm^2
Aspect ratio	ϵ	0.133	0.133	0.133
Reynolds number	Re	1.00	1.00	1.00
Bond number	Bo	0.72	0.72	0.72
Strain amplitude	Δ	0	0.1	0.1
Surface concentration ratio	Γ_0/Γ_1	0	0.42	0.8
Dimensionless well radius	$\hat{R}$	4.9	4.0	4.0

neglecting $O(\epsilon^2)$ and $O(Re\epsilon^2)$ terms in the momentum equation and the interfacial stress boundary condition, one obtains the following velocity field from the momentum and continuity equations, along with their boundary conditions.

$$u = Bo\left[\frac{1}{2}h_x z^2 - hh_x z\right] + \sigma_x z + V_{\text{wall}}$$
$$w = \frac{Bo}{x}\left(xh_x\left[\frac{z^2}{2}h - \frac{z^3}{6}\right]\right)_x - \frac{1}{x}\left(x\sigma_x\frac{z^2}{2}\right)_x - \frac{1}{x}\left(xV_{\text{wall}}\right)_x z \tag{7}$$

Inserting the velocity field and scalings into the kinematic boundary condition (Eq. 4) and surfactant conservation Eq. 3 results in the following evolution equations for film thickness and surfactant surface concentration, respectively.

$$h_t = \frac{1}{x}\left(x\left[\frac{Bo}{3}h^3h_x - \frac{h^2}{2}\sigma_x - V_{\text{wall}}h\right]\right)_x$$
$$\Gamma_t = \frac{1}{x}\left(x\left[\frac{1}{Pe}\Gamma_x - h\Gamma\sigma_\Gamma\Gamma_x + \frac{Bo}{2}\Gamma h^2h_x - \Gamma V_{\text{wall}}\right]\right)_x \tag{8}$$

For the uniform strain field used here, $V_{\text{wall}}=\xi R_t$, where ξ is a material coordinate attached to the membrane wall such that $x=\xi R(t)$. A specified value of ξ refers to a particular material point on the membrane wall at all times, where $\xi\subset[0, 1]$. In the no-stretch case, the radius of the domain, R, is constant, $\hat{R}$, and $V_{\text{wall}}=0$ at all x locations. In the wall stretch case, $R(t) = \hat{R}[1 + \Delta\sin(2\pi t/T_{C/V})]$, where Δ is the strain amplitude. The boundary conditions are no flux at the wall, $x=R$, and symmetry at $x=0$. To properly consider the solution near the wall (i.e., within one layer thickness), the governing equations should be re-scaled and this inner solution matched to the outer solution presented above. This would result in higher order corrections to the solution presented here. This inner region is neglected without impacting the leading order (in ϵ) solution considered in this work. The initial conditions for the evolution equations are

$$\Gamma(x,0) = \tfrac{1}{2}(\Gamma_1 - \Gamma_0)\{1 - \tanh[\alpha(x-1)]\} + \Gamma_0$$
$$h(x,0) = 1 \tag{9}$$

where α is an adjustable parameter chosen to approximate the step from Γ_1 to Γ_0 in the experiments, while allowing a smooth initial condition for Γ. The value of α was typically 500. The evolution equations are transformed to the material coordinate system and solved using the method of lines, with Gear's method temporally and central differences spatially. From this, we obtain the evolution of the film thickness, h, the evolution of surface concentration, Γ, and the velocity fields. By tracking the propagation of the surface particle that initially separates the new and pre-existing surfactants, we compute the location of the leading edge of the new surfactant front, $L_{\text{new}}(t)$, when the membrane is at its mean radius. Streamlines and vorticity fields are computed from the velocity field at eight times during one cycle.

4 Results

Figure 6 shows a comparison of film thickness measured in experiments using the constructed-light method and the theoretical predictions of film thickness $\Gamma_0^*=0$, and $\Gamma_1^*=4.24\times10^{-7}$ g/cm^2. The film thickness versus radial position is plotted for two different times. The symbols in Fig. 6 correspond to the mean of five experiments and the error bars indicate the standard error of the mean.

Figure 7 shows a plot of experimental and theoretical L_{new} versus time at several cycling periods for (Fig. 7a) $\Gamma_0/\Gamma_1=0.42$ and (Fig. 7b) $\Gamma_0/\Gamma_1=0.8$, where we use $\Gamma_1^*=4.24\times10^{-7}$ g/cm^2 for all the experiments. The symbols in Fig. 7 correspond to the mean of five experiments, and the error bars indicate the standard error of the mean. The lines indicate the theoretical prediction. Only the value of L_{new} when $R(t) = \hat{R}$ is shown for both the theoretical and experimental data, to allow comparison to the no-stretch case. For these pre-existing concentrations, stretching the mem-

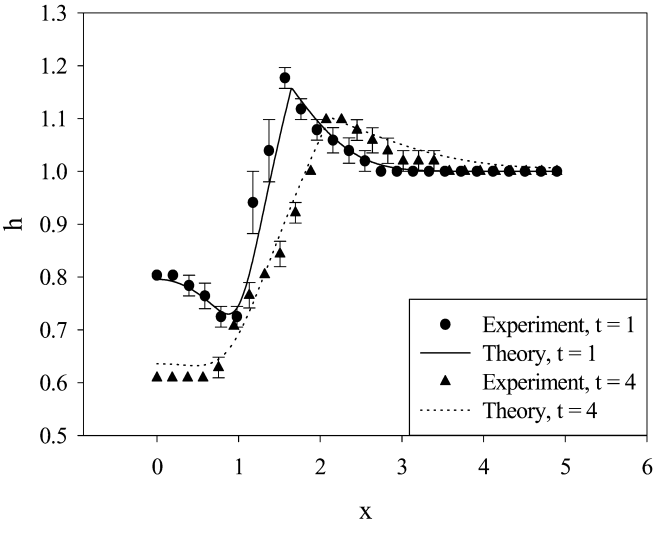

Fig. 6. Comparison of predicted and experimental film thickness, for h_0=2 mm, Γ^*_0=0, Γ^*_1=4.24×10^{-7} g/cm^2, at two non-dimensional times, t=1 and t=4

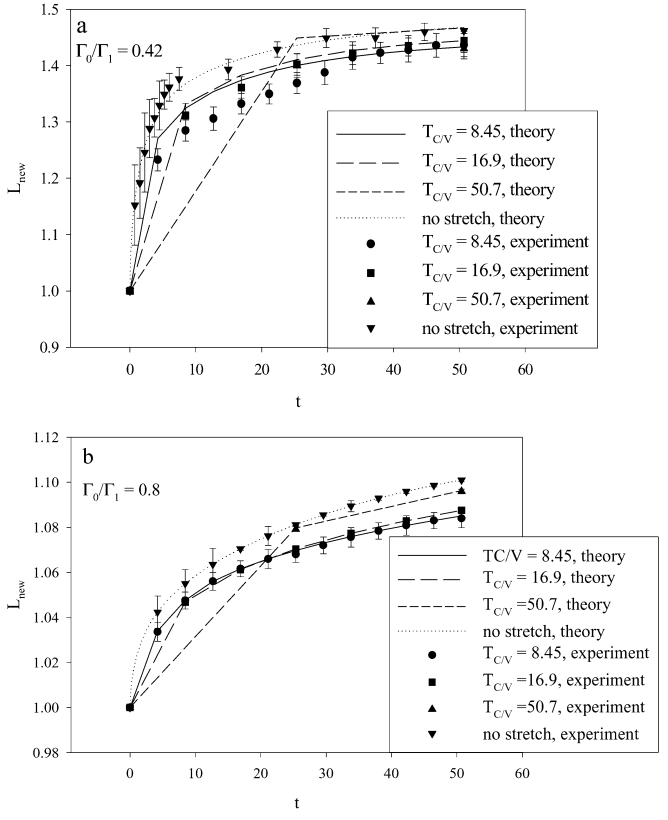

Fig. 7a, b. L_{new} vs t, comparison of theory and experiments, Δ=0.1. Data is only shown when membrane is at its mean radius (i.e. when $t=nT_{C/V}/2$, n=0, 1, 2, …). *Lines* indicate theory (*straight lines* connect values for which $R(t) = \hat{R}$, *symbols* indicate experiment. Γ_1^*=4.24×10^{-7} g/cm^2. a Γ_0/Γ_1=0.42, b Γ_0/Γ_1=0.8

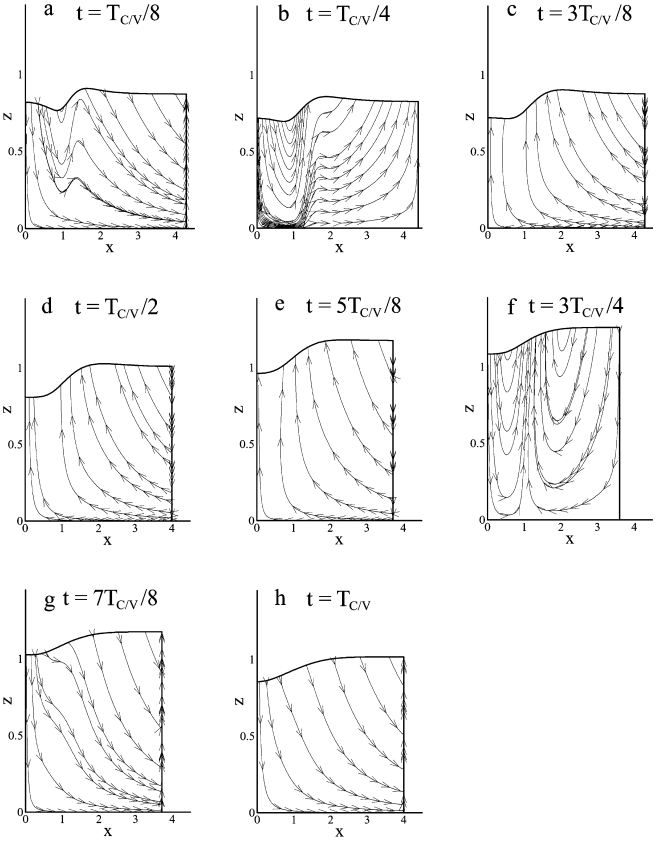

Fig. 8. Streamlines at different times in the first stretching cycle for Γ_0/Γ_1=0.42, Δ=0.1, $T_{C/V}$=8.45. Time is indicated on each frame

brane results in the new surfactant spreading at a slower rate than the no-stretch case for all stretching periods. Theoretical streamline evolution is shown for Γ_0/Γ_1=0.42 and Γ_0/Γ_1=0.8 in Figs. 8 and 9, respectively, for $T_{C/V}$=8.45. The streamline evolution is similar for the other cycling periods and is not shown. For a given Γ_0, the streamlines plots are considerably different depending on the time in cycle. When the membrane reaches its minimum length, two cells develop for Γ_0/Γ_1=0.42 and three cells develop for Γ_0/Γ_1=0.8. The film disturbance near the leading edge of the new surfactant front is considerably smaller for Γ_0/Γ_1=0.8 than for Γ_0/Γ_1=0.42 and damps out relatively quickly. Figures 10 and 11 show plots of the velocity field for the same times and surfactant concentrations as in Figs. 8 and 9, respectively. Figures 12 and 13 show Γ versus x for the same conditions and times. The position of the leading edge of the new surfactant front, L_{new}, is also shown in Figs. 12 and 13. The evolution of vorticity is shown in Figs. 14 and 15 for Γ_0/Γ_1=0.42 and Γ_0/Γ_1=0.8.

5
Discussion

5.1
Film thickness evolution

Figure 6 shows the evolution of the film thickness. There is good agreement between the theoretical predictions and the measured film thickness. This agreement suggests that the physics of the spreading are accurately reflected in the model. One would expect that if a different method of initiating the spreading was used, such as placing a drop on the interface, that the agreement between the measured and predicted film thicknesses would be decreased at early times. The surface wave propagates through the domain, with the crest of the wave near the leading edge of the new surfactant front. The wave height decreases as it propagates, making the measurement of the film thickness disturbance more difficult to resolve at later times. To ascertain that the removal of the restraining collar does not greatly influence the film thickness evolution, the constructed light was used with the removal of the collar without surfactant. The viscous film (glycerine) damped any disturbances created by the removal of the restraining collar almost instantaneously (within the first two frames of video). Thus, it does not appear that removing the collar influences the film thickness evolution substantially, provided some care is used in its removal.

While this film deformation is similar in appearance to a Reynolds ridge, a well-studied flow, and both deformations are brought about by the presence of surfactant, the mechanism that causes the film deformation observed here is different. The Reynolds ridge is a high-Reynolds-number phenomenon, which is not observed in Stokes flow (Harper 1992). The traditional Reynolds ridge is a deformation of the clean interface in front of a surfactant monolayer when the free stream flow is directed from the clean region towards the monolayer region. A boundary

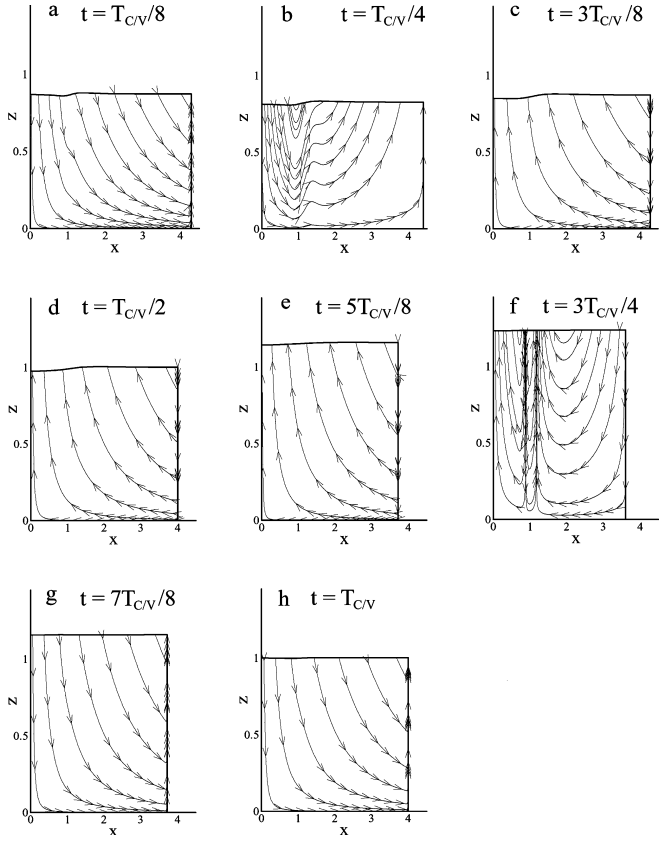

Fig. 9. Streamlines at different times in the first stretching cycle for Γ_0/Γ_1=0.8, Δ=0.1, $T_{C/V}$=8.45. Time is indicated on each frame

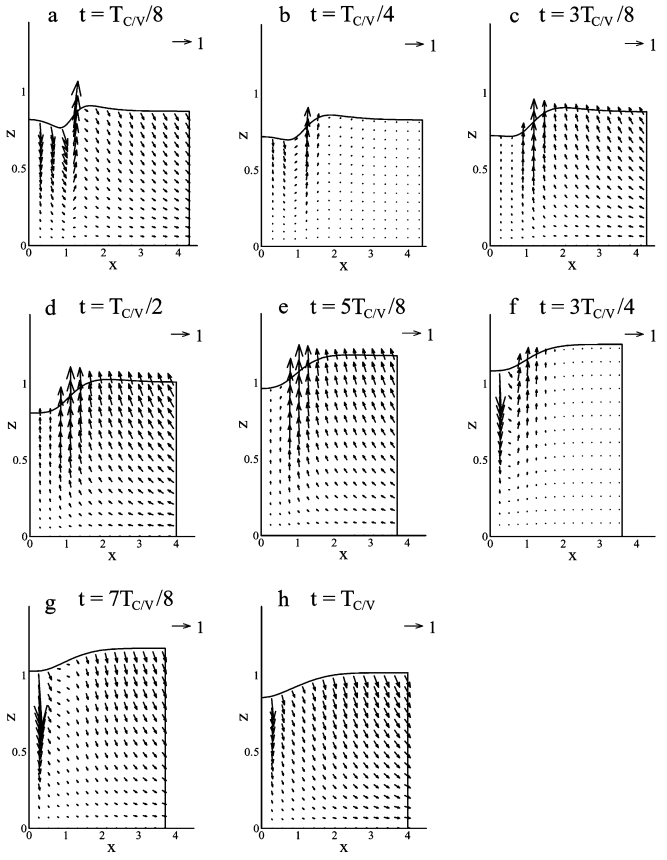

Fig. 10. Velocity field at different times in the first stretching cycle for Γ_0/Γ_1=0.42, Δ=0.1, $T_{C/V}$=8.45. Time is indicated on each frame

layer forms beneath the static monolayer (Harper and Dixon 1974; Scott 1982; Warncke et al. 1996). The thin-film Reynolds ridge develops due to inertially generated pressure fluctuations (Jensen 1998). The flows considered here are at low Reynolds numbers and this type of film deformation will occur in Stokes flow (Gaver and Grotberg 1990; Halpern and Grotberg 1992; Grotberg et al. 1995; Jensen and Halpern 1998; Bull et al. 1999). The deformation originates in spatially non-uniform fluxes of the liquid layer. Depending on the values of the Bond number, Peclet number, and pre-existing surfactant concentration, the film deformation is either partially or entirely under the new surfactant monolayer, whereas the Reynolds ridge occurs along the clean interface in front of the monolayer (Warncke et al. 1996). The experimental techniques that have been successfully used to investigate the Reynolds ridge appear applicable to this film deformation. For example, particle image velocimetry (Warncke et al. 1996) would provide velocity field information that could be compared to the theoretically predicted velocity field for these flows. The generated flows are important for the physiological application.

5.2
Membrane stretching

As shown in Fig. 7a for Γ_0=0.42Γ_1, spreading is fastest when there is no stretch. Smaller periods result in slower spreading. Similar trends are observed for Γ_0=0.8Γ_1 (Fig. 7b). However, for Γ_0=0.8Γ_1, the agreement between experiment and theory is slightly better, particularly for $T_{C/V}$=50.7. This is likely related to the accuracy of the isotherm. Although the variation in L_{new} with cycling period is not very large in these experiments, a dependence on cycling period is apparent. The largest effects of cycling on spreading rate are observed for $10<t<70$, suggesting that compression of the pre-existing surfactant and expansion of the new surfactant may limit the effects of the wall stretch on surface tension gradients. In the SRT, it is typical for the monolayer in small airways to be supplied with surfactant from the thicker surfactant layer in the large airways. In this situation, the effects of wall stretch may be greater.

The spreading rate dependence on cycling period is due to changes in viscous resistance (thickness changes), changes in surface tension gradients, and the fluid motion due to the wall motion. When the membrane is compressed, the surfactant concentration changes. Because the surfactant isotherm is non-linear and the area change with membrane stretch depends on the radial location, the changes in surface tension are different in the pre-existing surfactant region and the new surfactant region. This cycle dependence of the surface tension gradient which drives the flow results in differences in spreading rates seen in Fig. 7. If thinner films could have been used without rupture, one would expect the effects of wall stretch to be more pronounced, as the Bond number would have been smaller. For long times, the cycle-averaged L_{new} will asymptote to an equilibrium value that corresponds to a

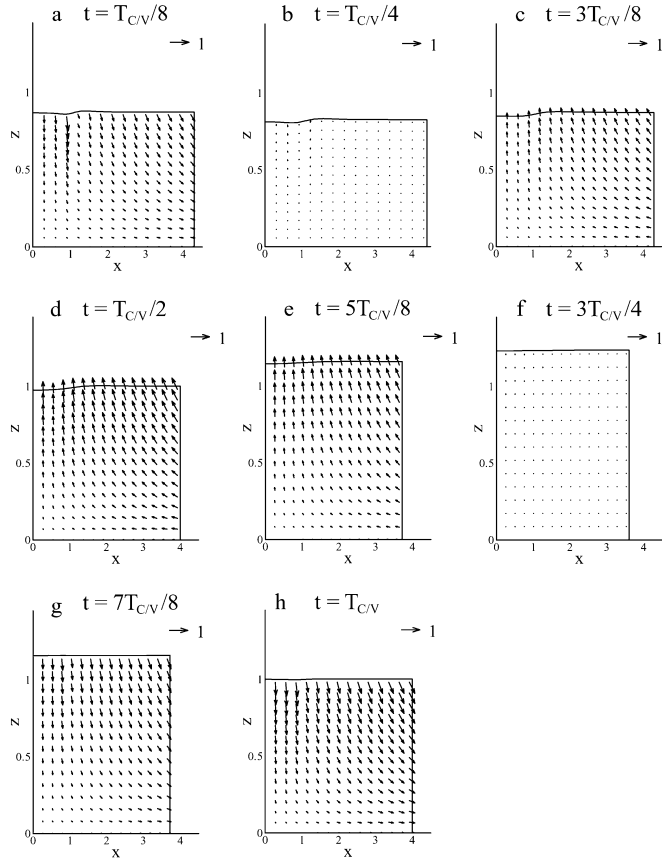

Fig. 11. Velocity field at different times in the first stretching cycle for Γ_0/Γ_1=0.8, Δ=0.1, $T_{C/V}$=8.45. Time is indicated on each frame

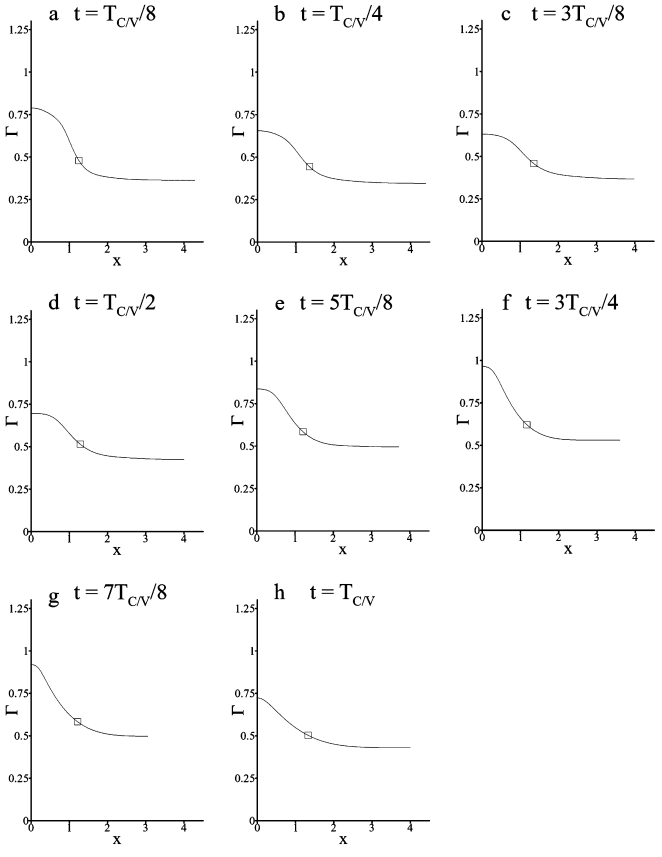

Fig. 12. Surfactant surface concentration, Γ, vs x at different times in the first stretching cycle for Γ_0/Γ_1=0.42, Δ=0.1, $T_{C/V}$=8.45. The radial position of the leading edge of the new surfactant front, L_{new} is indicated by an *open square*. Time is indicated on each frame

uniform cycle-averaged surface tension throughout the film. This value is in general different for all stretching periods, assuming surface diffusion is negligible and the surfactant isotherm is non-linear. However, the value of L_{new} as $t\to\infty$ is similar for all periods for the experiments considered here. Nevertheless, this method has considerable potential for the experimental investigation of situations where the periodic wall stretch has a substantial effect. For example, lung surfactant has a more non-linear isotherm (Schurch et al. 1989) than the surfactant considered here and its solubility adds many interesting effects, due to sorption kinetics, not seen with the insoluble surfactant considered here. The close agreement between experiment and theory presented in this work suggests that the model is accurate and captures the relevant physics.

The motion of the fluid due to the competition between wall stretch and surface tension gradients is apparent from the streamline plots in Figs. 8 and 9. These plots show one cycle of membrane stretching for $T_{C/V}$=8.45 and Δ=0.1. When the membrane lengthens at the start of the cycle, the fluid motion is generally in the positive x direction (Figs. 8 and 9, a and b). When the membrane shortens, the motion changes direction, except very near the film disturbance in Fig. 9c and e. When the membrane is at its shortest length, vortices form in the streamline plots (Figs. 8f and 9f). As the membrane lengthens, the flow becomes directed primarily in the positive x direction (Figs. 8 and 9, g and h). The film thickness disturbance is considerably smaller for Γ_0=0.8Γ_1 than for Γ_0=0.42Γ_1, since the surface tension gradient driving the flow is considerably smaller. Because of this smaller surface tension gradient, the new surfactant spreads slower and a shorter distance than for Γ_0=0.42Γ_1. This competition between wall stretch and surface tension gradients is apparent in the velocity fields of Figs. 10 and 11, which are for the same conditions as Figs. 8 and 9, respectively. The surface concentration of surfactant is shown in Figs. 12 and 13 at the same times as the velocity fields in Figs. 10 and 11. At time t=0, the membrane well is at its mean radius, and new surfactant spreading and membrane wall stretch begin. At early times in the initial stretching cycle, the surface tension gradients are larger than at later times. This results in larger velocities near the surface in the new surfactant region ($x<L_{new}$). The surface tension gradient in the pre-existing surfactant region ($x>L_{new}$) is not as large, as the surfactant concentration has less spatial variation here at a given time. Wall stretch influences the flow both through the lower boundary and through the compression and expansion effects it has on the interface. In Fig. 10a ($t=T_{C/V}/8$), the membrane is lengthening and the highest velocities occur at the surface of the film in the vicinity of the leading edge of the new surfactant front, which lies near the crest of the film deformation in the absence of wall stretch. The velocities are in the negative z direction in much of the fluid, except near

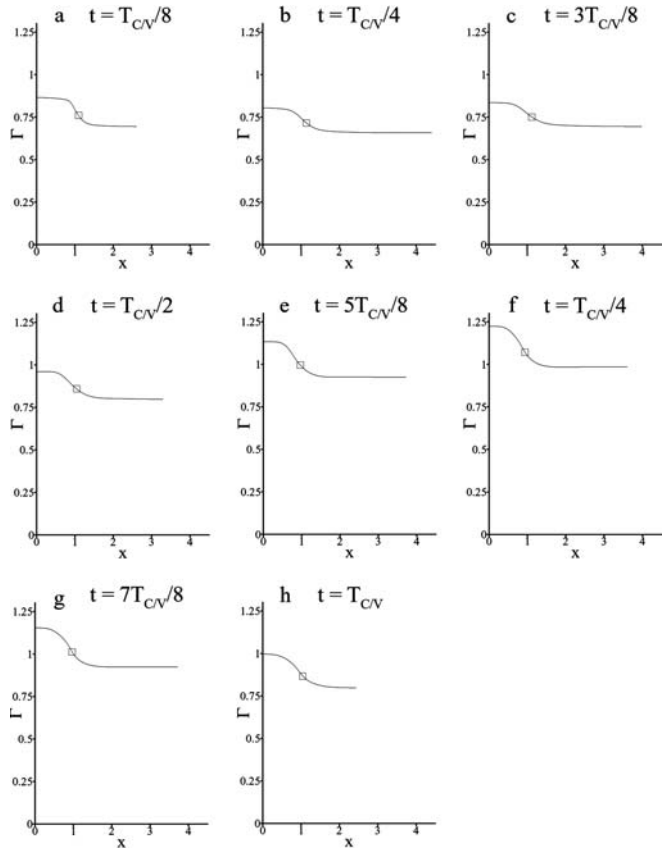

Fig. 13. Surfactant surface concentration, Γ, vs x at different times in the first stretching cycle for Γ_0/Γ_1=0.8, Δ=0.1, $T_{C/V}$=8.45. The radial position of the leading edge of the new surfactant front, L_{new} is indicated byan *open square*. Time is indicated on each frame

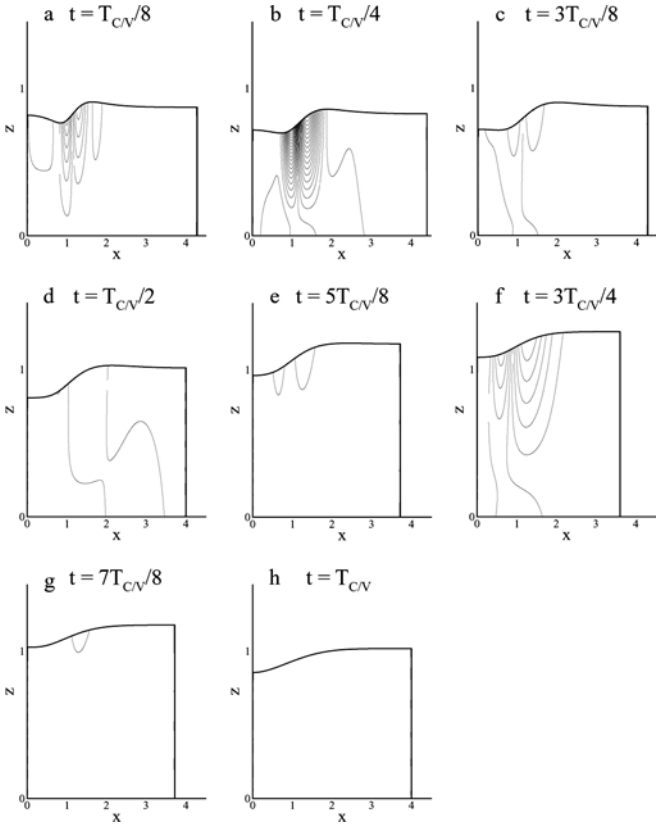

Fig. 14. Contours of constant vorticity at different times in the first stretching cycle for Γ_0/Γ_1=0.42, Δ=0.1, $T_{C/V}$=8.45. Time is indicated on each frame

the film deformation, reflecting that the film is thinning due to the increasing membrane well radius.

When the membrane well reaches its largest radius and begins to shorten (Fig. 10b, t=$T_{C/V}$/4), the wall velocity is zero and the velocity field primarily shows the effects of the surface tension gradients. There is some fluid inertia in this system, as Re≈1. When the radius of the well is decreasing (Fig. 10c–e, t=3$T_{C/V}$/8, t=$T_{C/V}$/2, and t=5$T_{C/V}$/8), the velocities at locations away from the bottom wall have a positive z-component because the film thickens. The surface velocities in the pre-existing region are in the negative x-direction due to the motion of the lower wall and the surface compression effect of the motion of the right boundary. The surface velocities in the new surfactant region have a small positive x-component due to the surface tension gradient. The location of the maximum surface velocity shifts to the left as the radius of the domain becomes smaller and the surface becomes compressed. At t=3$T_{C/V}$/4 (Fig. 10f), the wall velocity changes sign (the radius is at its minimum at this time) and the effect of the surface tension gradient is seen near the surface in the new surfactant region. The flow is such that the film thickens near the leading edge of the new surfactant front and thins behind it. The velocities at locations in the pre-existing region when t=3$T_{C/V}$/4 are very small. As the membrane radius increases back to its initial radius (Fig. 10f and h), the flow near the bottom wall and the flow in the pre-existing surfactant region exhibit primarily the effects of the wall motion. The flow in the upper half of the film in the new surfactant region is strongly influenced by the surface tension gradient there. Far to the right of the leading edge of the new surfactant front, the surface tension gradients are smaller and consequently their effect is not as strong. Away from the surface, the effects of the surface tension gradient are not as pronounced and the wall motion appears to dominate the flow there.

The velocity fields for Γ_0/Γ_1=0.8 (Fig. 11) are influenced by the same wall motion as the velocity fields for Γ_0/Γ_1=0.42 (Fig. 10), but the surface tension gradients are smaller. Consequently, the velocities at locations in the new surfactant region are more strongly influenced by the wall motion. Note that the slope of the surfactant isotherm, shown in Fig. 2, is smaller for higher values of Γ, such as those near Γ_0/Γ_1=0.8, where Γ_1^*=4.24×10^{-7} g/cm^2. In the first half of the cycle (Fig. 11a–d), there is a film deformation, which is smaller than that in Fig. 10 since the surface tension gradient responsible for it is smaller. As time progresses, the film deformation decreases in height as the new surfactant spreads and consequently the surface tension gradient decreases. By the time t=3$T_{C/V}$/4 (Fig. 11f), the film deformation has nearly disappeared and the velocity is nearly uniform as the wall velocity is zero at this time and the membrane well radius is at its minimum. The subsequent lengthening of the radius (Fig. 11g and h) results in flow that is primarily dominated by the wall motion with some effects of surface tension gradients induced by the expansion of the interface. Even

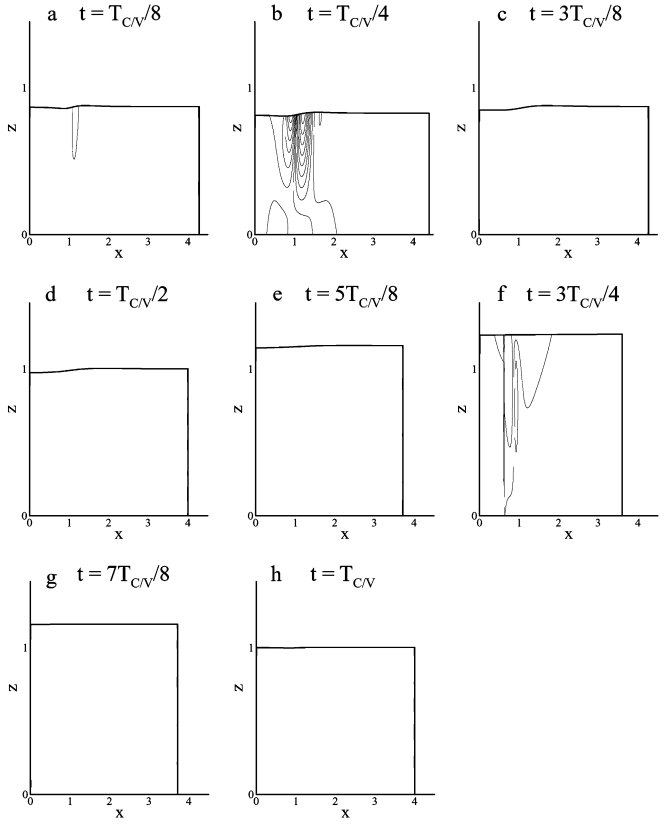

Fig. 15. Contours of constant vorticity at different times in the first stretching cycle for Γ_0/Γ_1=0.42, Δ=0.1, $T_{C/V}$=8.45. Time is indicated on each frame

for no initial surface tension gradient, wall stretch can induce surface tension gradients through the expansion and compression of the interface.

Figures 14 and 15 show vorticity plots for the same conditions as Fig. 8 and 9, respectively. As in Figs. 8, 9, 10, 11, these figures show several times during a cycle. The primary source of vorticity appears to be the interaction of surface tension gradients with wall motion to produce spatial variations in velocity. Consequently, the vorticity contours are more closely spaced near the new surfactant region when the surface tension gradient is large (Fig. 14a and b). Likewise in Fig. 14h, there is much less vorticity than at earlier times because the new surfactant has spread and the film deformation has decreased in height.
Figure 15 shows that when the surface tension gradient is weak, little vorticity is generated. However, changing the sign of the wall velocity can generate vorticity in this system (Fig. 15b and f, and Fig. 14b and f).

The flows that results from periodic wall stretch are important in the transport of large molecules, passive solute transport, e.g., genetic material in gene therapy, gas transport in partial liquid ventilation, cell-to-cell signaling, or surfactant transport between the interface and the membrane wall. The regions of recirculation that develop at certain times during the cycle may be important in the transport of messengers between cells in a normal lung. The type of experiment presented here could be used to investigate these important physiological flows in a benchtop setting.

5.3 Conclusions

We have presented experimental methods for measuring film thickness and for studying the effects of wall stretch in surfactant-spreading experiments. Both of these methods are effective and their results agree with the current theoretical models. These methods will likely be instrumental in further experimental investigations of monolayer spreading on thin films (for the pulmonary application discussed here and for other non-physiological applications) and investigation of the effects of wall stretch on many bio-fluid phenomena besides surfactant phenomena.

References

Adamson AW (1990) Physical chemistry of surfaces. Wiley-Interscience, New York

Borgas MS, Grotberg JB (1988) Monolayer flow on a thin film. J Fluid Mech 193:151–170

Bull JL (2000) Surfactant and liquid transport in a thin viscous film with pre-existing surfactant and periodic wall stretch. PhD thesis. Northwestern University, Evanston, Ill.

Bull JL, Nelson LK, Walsh JT, Glucksberg MR, Schurch S, Grotberg JB (1999) Surfactant-spreading and surface-compression disturbance on a thin viscous film. J Biomech Eng Trans ASME 121:89–98

Cassidy KJ, Halpern D, Ressler BG, Grotberg JB (1999) Surfactant effects in model airway closure experiments. J Appl Physiol 87:415–427

Davis SH, Liu A-K, Sealy GR (1974) Motion driven by surface-tension gradients in a tube lining. J Fluid Mech 62:737–752

Espinosa FF, Kamm RD (1997) Thin layer flows due to surface tension gradients over a membrane undergoing non-uniform, periodic strain. Ann Biomed Eng 25:913–925

Espinosa FF, Kamm RD (1999) Bolus dispersal through the lungs in surfactant replacement therapy. J Appl Physiol 86:391–410

Espinosa FF, Shapiro AH, Fredberg JJ, Kamm RD (1993) Spreading of exogenous surfactant in an airway. J Appl Physiol 75:2028–2039

Gaver DP, Grotberg JB (1990) The dynamics of a localized surfactant on a thin film. J Fluid Mech 213:127–148

Gaver DP, Grotberg JB (1992) Droplet spreading on a thin viscous film. J Fluid Mech 235:399–414

Grotberg JB (1994) Pulmonary flow and transport phenomena. In: Lumley JL, Dyke M Van, Reed HL (eds) Annual Reviews of Fluid Mechanics. Annual Reviews, Palo Alto, Calif., pp 529–571

Grotberg JB, Halpern D, Jensen OE (1995) Interaction of exogenous and endogenous surfactant: spreading-rate effects. J Appl Physiol 78:750–756

Halpern D, Grotberg JB (1992) Dynamics and transport of a localized soluble surfactant on a thin film. J Fluid Mech 237:1–11

Halpern D, Grotberg JB (1993a) Surface tension instabilities of liquid-lined elastic tubes. In: Cheers AY, Dam CP van (eds) Contemporary mathematics (fluid dynamics in biology). American Mathematical Society, Providence, R.I., pp 295–316

Halpern D, Grotberg JB (1993b) Surfactant effects on fluid-elastic instabilities of liquid-lined flexible tubes: a model of airway closure. J Biomech Eng Trans ASME 115:271–277

Halpern D, Grotberg JB (1999) Oscillatory shear stress induced stabilization of thin film instabilities. In: Chang H-C (ed) IUTAM Symposium on nonlinear waves in multiphase flow, 1999. Kluwer, Dordrecht, pp 33–43

Halpern D, Hamer B, Grotberg JB (1993) Capillary-elastic instabilities of liquid-lined flexible tubes: a model of airway closure. In: Tarbell JM (ed) Advances in bioengineering (Proceedings of the ASME, BED), 1993, pp 223–226

Halpern D, Jensen OE, Grotberg JB (1998a) A theoretical study of surfactant and liquid delivery into the lung. J Appl Physiol 85:333–352

Halpern D, Moriarty JA, Grotberg JB (1998b) Capillary-elastic instabilities with an oscillatory forcing function. In: Durban D, Pearson JRA (eds) IUTAM Symposium on non-linear singularities in feformation and flow, 1998. Kluwer, Dordrecht, pp 243–255

Harper JF (1992) The leading edge of an oil slick, soap film, or bubble stagnant cap in Stokes flow. J Fluid Mech 237:23–32
Harper JF, Dixon JN (1974) The leading edge of a surface film on contaminated flowing water. In: Harper JF, Dixon JN (eds) Proceedings of the 5th Australasian conference on hyrdraulics and fluid mechanics, 9–13 December, 1974, Christchurch, New Zealand, pp 499–505
Jensen OE (1998) The stress singularity in surfactant-driven thin-film flows. Part 2. Inertial effects. J Fluid Mech 372:301-322
Jensen OE, Grotberg JB (1992) Insoluble surfactant spreading on a thin viscous film: shock evolution and film rupture. J Fluid Mech 240:259–288
Jensen OE, Grotberg JB (1993) The spreading of heat or soluble surfactant on a thin liquid film. Phys Fluids A (Fluid Dyn) 5:58–68
Jensen OE, Halpern D (1998) The stress singularity in surfactant-driven thin-film flows. Part 1. Viscous effects. J Fluid Mech 372:273–300
Jensen OE, Halpern D, Grotberg JB (1994) Transport of a passive solute by surfactant-driven flows. Chem Eng Sci 49:1107–1117
Keshgi HS, Scriven LE (1991) Dewetting, nucleation and growth of dry regions. Chem Eng Sci 46:519–526
Schurch S, Bachofen H, Goerke J, Possmayer F (1989) A captive bubble method reproduces the in situ behavior of lung surfactant monolayers. J Appl Physiol 67:2389–2396
Scott JC (1982) Flow beneath a stagnant film on water: the Reynolds ridge. J Fluid Mech 116:283–296
Shen H, Hartland S (1994) Effect of interfacial concentration gradients of insoluble surfactants on local film-thinning. J Coll Interface Sci 167:94–103
Troian SM, Herbolzheimer E, Safran SAPRL (1990) Model for the fingering instability of spreading surfactant drops. Phys Rev Lett 65:333–336
Warncke A, Gharib M, Roesgen T (1996) Flow measurements near a Reynolds ridge. J Fluids Eng 118:621–624
Weh L, Linde H (1973) Kraterförmige Oberflächenstraungen in Anstrichfilmen, verursacht durch Silikonlzusätze. Plaste Kautsch 20:849–860